Research Paper

One-dimensional mathematical modeling of two-phase ejectors: Extension to mixtures and mapping of the local exergy destruction

Øivind Wilhelmsen [a,b,*], Ailo Aasen [b], Krzysztof Banasiak [b], Halvor Herlyng [c], Armin Hafner [c]

[a] *NTNU, Department of Chemistry, Høgskoleringen 5, NO-7491 Trondheim, Norway*
[b] *SINTEF Energy Research, Sem Sælands vei 11, NO-7034 Trondheim, Norway*
[c] *NTNU, Department of Energy and Process Engineering, Kolbjørn Hejes vei 1, NO-7491, Trondheim, Norway*

A R T I C L E   I N F O

A B S T R A C T

The ejector is a process equipment frequently used in refrigeration processes. There is currently a knowledge gap on the efficiency of ejectors operating with mixtures. To address this knowledge gap, we present a one-dimensional ejector model for mixtures, defined by spatially distributed mass-, energy- and momentum-balances for different zones, which together constitute the full ejector geometry. The recently developed delayed homogeneous relaxation model is used to describe the two-phase transition in the motive and suction nozzles. For evaporation of pure CO_2 in the throat of the motive nozzle, the model yields an average error of 2.6% in the critical mass flow rate, which is significantly lower than the homogeneous equilibrium model that has an average error of 8.4%. A comparison to new experimental data shows that both models give excellent predictions of critical mass flow rates where condensation occurs in the throat, with an average error below 0.9%. New experimental data with CO_2 are presented, which are used to regress two parameters in correlations that describe the momentum transfer between the primary and secondary stream in the mixer and diffuser sections. This leads to accurate reproduction of the pressure lift in five different ejector geometries, with a mean error of 2.3%. By using nonequilibrium thermodynamics, we derive formulae for the local exergy destruction in the ejector. The largest exergy destruction is located in the mixer, and originates in transfer of momentum between the primary and secondary streams. The local exergy destruction profiles through the mixer and diffuser are highly non-uniform, and deviate from the established guidelines for energy-efficient design characterized by equipartition of exergy destruction. This reveals a potential to increase the performance of ejectors by suitable adjustments to their geometric design. The mathematical model validated for pure CO_2 is assumed to also be valid for mixtures rich in CO_2. We show that minute concentrations of a second component can have a significant influence on the ejector performance. When fixing the inlet conditions and ejector geometry, we demonstrate that adding 2% H_2 to a mixture of CO_2 decreases the critical mass flow rate by 20%, while adding 2% SO_2 increases the pressure lift by 1 bar.

1. Introduction

Ejectors are frequently used in refrigeration processes due to their lack of moving parts, limited maintenance and low investment cost [1]. In an ejector, the primary, high-pressure stream is sent through a nozzle to accelerate it and decrease its pressure. This sucks in a secondary, low-pressure stream, entrains it, and increases its pressure. By increasing the pressure of the secondary stream, part of the pressure-volume work of the primary stream can be recovered [2]. The increase in pressure of the secondary stream is referred to as the pressure-lift, and together with the ejector efficiency [3], they constitute important performance indicators of ejectors. Liu reviewed ejector efficiencies in various ejector systems [4], and found numbers that varied between

5% and 40% depending on the application. Since the ejector is a key source of exergy destruction in e.g. ejector chillers driven by solar heat [5,6] as well as other applications [1], there is a need to increase their efficiencies and thus reduce the dissipation of useful work.

Entropy generation analysis [7] is a powerful tool to extract details on how useful work is dissipated in process-equipment. The approach has for example been used to gain insight into chemical reactors [8], distillation columns [9] and heat exchangers [10,11]. Such analyses have also been applied to ejectors. Sierra-Pallares et al. used computational fluid dynamics (CFD) simulations to study the mechanisms of entropy generation in ejectors with different geometries and operating conditions [12]. They found that viscous dissipation is responsible for

Nomenclature

Abbreviations

D-HRM	Delayed Homogeneous Relaxation Model
HEM	Homogeneous Equilibrium Model

Greek symbols

β	Vapor mass fraction (–)
ϵ	Roughness (m)
η	Dynamic viscosity (kg m^{-1} s^{-1})
Γ	Mass transfer rate (kg s^{-1})
γ	Angle (°)
μ	Chemical potential (J kg^{-1})
Π	Momentum transfer rate (kg m s^{-2})
ρ	Density (kg m^{-3})
σ	Local entropy production (W m^{-1} K^{-1})
τ	Relaxation time (s)

Roman symbols

A	Area (m^2)
a	Momentum transfer parameter (–)
C	Drag coefficient in Eq. (34) (–)
D	Diameter (m)
$\dot{e}_d$	Local exergy destruction (W/m)
$\dot{E}_d$	Integrated exergy destruction (W)
f	Fanning friction factor (–)
f_c	Source term in mass balance (kg m^{-1} s^{-1})
f_e	Source term in energy balance (J m^{-1} s^{-1})
f_m	Source term in momentum balance (kg s^{-2})
h	Specific enthalpy (J kg^{-1})
L	Length (m)
$\dot{m}$	Mass flow rate (kg s^{-1})
N	Number of components in mixture (–)
P	Pressure (Pa)
Re	Reynolds number (–)
r	Radius (m)
s	Specific entropy (J kg^{-1} K^{-1})
T	Temperature (K)
u	Uncertainty of measurement
v	Flow speed (m s^{-1})
w_i	Mass fraction of component i (–)
W	Force (kg m s^{-2})
X	Liquid mass fractions (–)
Y	Vapor mass fractions (–)
Z	Total mass fractions (–)
z	Spatial coordinate (m)

Subscripts and superscripts

DIF	Diffuser
EoS	Equation of state

I	Primary (motive) flow
II	Secondary (suction) flow
in	Inlet
int	Interface between primary and secondary flow
liq	Liquid phase
MCH	Pre-mixing chamber
MIX	Mixer
MN	Motive nozzle
out	Outlet
sat	Saturated
SN	Suction nozzle
vap	Vapor phase
w	Wall

reduce irreversibilities and increase the efficiency of refrigeration processes. The vast majority of the research on ejectors, however, has been devoted to single-component systems [4], with some exceptions [17, 18]. In particular, previous works on entropy generation analysis in ejectors have only considered single-component fluids. For mixtures, new modes of entropy generation from e.g. mixing phenomena can lead to a reduction in efficiency. Hence, there is a need to gain further insight on how mixtures behave in ejectors, and in particular how the composition affects their performance.

Ejectors host a myriad of physical phenomena. While the primary and secondary streams may be single-phase as they enter the ejector, phase change is likely to occur after the nozzle throat [2]. Furthermore, a shock may form downstream [13], where wall-interactions, entrainment and mixing effects influence the performance of the ejector. Theoretical studies of ejectors in the literature have been carried out at several levels of complexity. The simplest type of models presented in the literature represent the different regions of the ejector with algebraic equations [13], in combination with assumed efficiencies for the different segments of the ejector [5]. This approach may be suitable if the efficiencies are well-known. However, these models offer little predictive ability about the ejector performance beyond this. Another approach is to represent the different zones in the ejector by suitable equations for mass-, energy- and momentum-balances, combined with a thermodynamic description and closure relations. Banasiak and Hafner [2] presented a one-dimensional, steady-state model of an ejector for CO_2. They achieved excellent agreement with experimental data, with an average deviation of 2.66% for the pressure lift, and 1.84% for the predicted mass flow rate. This type of model can give much insight on the design and efficiency of ejectors, with the main limitation being that the correlation used to describe how the primary and secondary streams exchange momentum has parameters that can vary from fluid to fluid. To overcome this challenge, it is possible to use two or three-dimensional CFD models, where further details are resolved [12,19].

Motivated by the present knowledge gap in the literature on the efficiency of ejectors operating with mixtures, the main innovation of the present work is the development of a one-dimensional spatially distributed ejector model that can be used to analyze the entropy generation for ejectors operating with mixtures. We present a methodology for mapping the local exergy destruction in the ejector such that the key sources of irreversibility can be identified and handled appropriately. In addition, new experimental results are presented for pure CO_2, which are used to improve the accuracy of the model and to strengthen conclusions made in previous work [20]. Computational efficiency combined with a high accuracy make the model well suited for incorporation in complex process schemes or optimization studies.

The article is structured as follows. The mathematical ejector model is presented in Section 2 along with details on how the system of equations has been solved. Next, the experimental campaign is described in
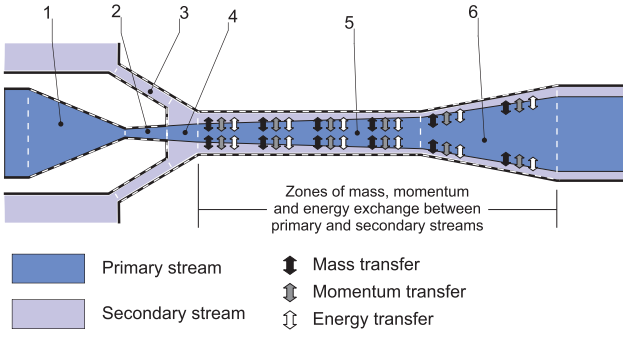
more than 75% of the total entropy production, and argued that the geometry of the ejector can provide a handle to improve the efficiency. Other authors have also studied the entropy generation in ejectors and have come to similar conclusions [13–15].

It is well-known from e.g. research on liquefaction of natural gas, that the use of mixed refrigerants with optimized compositions [16] can

Fig. 1. The six computational zones for the ejector model: (1) The converging (subsonic) section of the motive nozzle, (2) the diverging (supersonic) section of the motive nozzle, (3) the suction nozzle, (4) the pre-mixing chamber, (5) the mixer, (6) the diffuser.

Section 3 before results and conclusions are provided in Sections 4 and 5 respectively.

2. Ejector model

In this section, we will present a mathematical model of an ejector that can handle mixtures in the single- and two-phase regimes. We shall also present equations to compute the local entropy production/exergy destruction. The model is developed by dividing the ejector into six zones, as shown in Fig. 1. The figure shows that the ejector consists of two streams, where the primary stream (high pressure, dark shaded) enters into the motive nozzle in Zone 1, and the secondary stream enters into the suction nozzle in Zone 3 (low pressure, light shaded). They start to interact in Zone 4 and exchange mass, momentum and energy in Zones 5 (the mixer) and 6 (the diffuser).

A typical geometry of an ejector is depicted in Fig. 2. The type of ejector considered in this work can be described by seven diameters (D), five angles (γ), and two lengths (L), where the subscripts denote their location in the ejector where subscript MN is short for motive nozzle, SN is the suction nozzle, MCH is the pre-mixing chamber, MIX is the mixer and DIF is the diffuser. These parameters are used to calculate the length, L_i and cross-sectional area, $A_i(z_i)$ of Zone i, where z_i denotes the spatial dimension of Zone i. The cross-sectional area of Zone i is perpendicular to the direction of z_i. We employ a plug-flow formulation in each zone, meaning that all properties are assumed to be perfectly mixed and uniform across the cross-sectional area. The link between the geometry specifications shown in Fig. 2 and the relevant variables in the differential equations, L_i and $A_i(z_i)$, are derived in the Supplementary Material. We shall next present the balance equations for each zone.

2.1. Mathematical modeling of Zones 1–3

In Zones 1–3, we assume that we have either single- or two-phase flow that is homogeneously distributed across the cross-sectional area. We shall use area-averaged equations to describe the behavior of these streams, as derived in Section 1.2.6 of Ref. [21]. The continuity equation of these sections is

$$\frac{d(A\rho v)}{dz} = \frac{d\dot{m}_{\text{tot}}}{dz} = 0, \tag{1}$$

where A is the area, ρ is the area-averaged density, v is the velocity in the flow direction, $\dot{m}_{\text{tot}}$ is the total mass flow rate and z is the spatial coordinate in the flow direction. The momentum balance is

$$\frac{d\left(A\left(\rho v^2 + P\right)\right)}{dz} = P\frac{dA}{dz} - \frac{f\rho v^2}{8}\frac{dA_w}{dz} \tag{2}$$

where f is Fanning's friction factor, P is the pressure and dA_w/dz is the differential wall surface area per length. The two-phase viscosity

was approximated according to the effective medium theory. This theory was originally derived for the mean thermal conductivity and successfully tested by Awad and Muzychka [22] for the mean viscosity of vapor–liquid mixtures for various refrigerants. The friction factor f was predicted by the empirical correlation by Churchill [23]. The energy balance is

$$\frac{d\left(A\rho v\left(h + \frac{v^2}{2}\right)\right)}{dz} = 0 \quad \rightarrow \quad \frac{d\left(h + \frac{v^2}{2}\right)}{dz} = 0 \tag{3}$$

where h is the mass-specific enthalpy of the mixture. We have here neglected a possible heat flux from the walls, which is justified by the time scale for heat transfer being short compared to typical flow speeds and ejector dimensions. These equations were solved self-consistently at each spatial position.

The system Eqs. (1)–(3) comprises three equations for the four quantities (v, ρ, P, h), which will be closed with a relation between the thermodynamic properties (ρ, P, h). This work will consider two closures: the homogeneous equilibrium model, and a nonequilibrium relaxation model.

2.1.1. The homogeneous equilibrium model

In the homogeneous equilibrium model (HEM), the closure is accomplished by assuming thermodynamic equilibrium at all states along the flow path. This entails solving one algebraic equation at every spatial step in the integration of the ordinary differential equations. With an initial guess for the velocity one can compute h and P by use of Eqs. (2) and (3). An enthalpy–pressure flash calculation is then used to identify the temperature, vapor fraction and compositions in each phase. By using an equation of state, the density ρ_{EoS} is thus computed. Furthermore, ρ is next computed from Eq. (1), yielding $\dot{m}_{\text{tot}}/Av$. At every spatial position we require in the HEM model that the following residual is zero

$$\text{res} = \rho_{\text{EoS}}(h, P) - \frac{\dot{m}_{\text{tot}}}{Av}. \tag{4}$$

2.1.2. The delayed homogeneous relaxation model

As shown by Banasiak et al. [2], HEM leads to an underestimation of the maximum mass flow rate of liquid that the motive nozzle can accommodate. The reason is that HEM assumes that the phase transition starts the moment the liquid becomes saturated, whereas in practice the phase transition is delayed as the liquid will persist for some time in a single-phase metastable regime. Accounting for this will increase the critical mass flow rate of liquid beyond the value given by HEM. In a recent work [20], we presented the delayed homogeneous relaxation model (D-HRM), which was shown to reproduce experimental critical mass flow rate with a higher accuracy than other methods for CO_2, without the need for fitting parameters [20,24]. In the following, we will show how to incorporate the D-HRM into the ejector model and extend previous modeling efforts to mixtures.

For a metastable fluid, we define the degree of metastability as

$$\Delta T(P) = T_{\text{m}}(P) - T_{\text{sat}}(P), \tag{5}$$

where T_{m} is the temperature of the metastable fluid phase and T_{sat} is the temperature of the saturated fluid phase at the same pressure P. The quantity ΔT is positive for evaporation and negative for condensation, and its extremum, ΔT_{lim}, corresponds to the nucleation limit for evaporation or condensation.

The nucleation limit ΔT_{lim} of a fluid mixture can be predicted by use of homogeneous nucleation theory [24], which works well at sufficiently high reduced temperatures [20]. At temperatures close to the critical temperature, we shall employ the same theory as presented by Aursand et al. [24]. At lower temperatures, there is a need to use heterogeneous nucleation theory, since the activation energy to initiate the phase change is lowered by cracks and imperfections at the nozzle structure. Further details on the computation of ΔT_{lim} for homogeneous and heterogeneous nucleation can be found in Ref. [20].
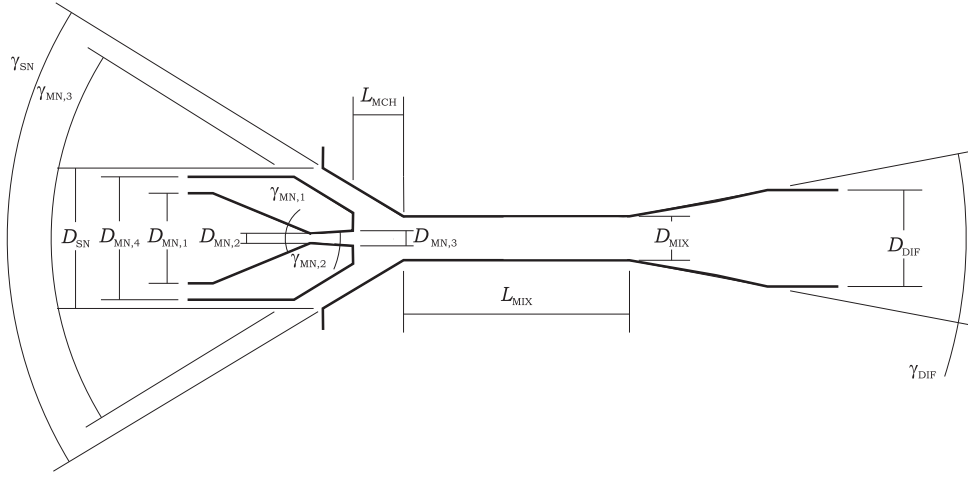
Fig. 2. A schematic sketch of the geometry of the ejector model that has been implemented. The ejector was manufactured in two separate pieces: (1) the motive nozzle, (2) suction nozzle, mixer, and diffuser.

A crucial parameter in the determination of the nucleation limit ΔT_{lim} is the vapor–liquid surface tension. For pure fluids the surface tension is usually tabulated. For mixtures this is rarely the case, but it can be estimated, for example, using density gradient theory with a geometrical mixing rule based on the pure component parameters (see Refs. [25–27] for further details). For simplicity, this work will use the HEM for mixtures.

As the single-phase fluid flows towards the throat, it eventually becomes metastable and ΔT starts approaching the nucleation limit. At some location z_l the metastability of the liquid matches ΔT_{lim}, that is

$$\Delta T(P(z_l)) = \Delta T_{\text{lim}}(P(z_l)). \tag{6}$$

At this location the nonequilibrium phase change process starts, by which the metastable single-phase fluid relaxes towards a two-phase equilibrium. As in previous work [20], we have used the simple relaxation model

$$\frac{d\Delta T}{dt} = -\frac{\Delta T}{\tau}, \tag{7}$$

where $\tau = 10^{-4}$ s. Eq. (7) can readily be replaced by a more sophisticated relaxation model that includes a possible dependence on the fluid state. However, we have found that the exact value of τ has a small/negligible influence on the predicted critical mass flow rates. The choice $\tau = 10^{-4}$ s was found to be a good compromise between numerical problems for $\tau \lesssim 10^{-6}$ s, and an essentially frozen degree of metastability when $\tau \gtrsim 10^{-2}$ s.

Before the nucleation limit is reached, the thermodynamic properties are computed as that of a pure fluid. In the relaxation regime, we can compute extensive properties as a sum of extensive properties of the phases, where we assume that the incipient phase is saturated. In both cases the appropriate consistency criteria are given by requiring that the following residuals are zero, where we for concreteness consider an evaporating flow:

$$\text{res}_1 = \beta/\rho_{\text{EoS}}^{\text{vap}}(T^{\text{sat}}(P), P, \mathbf{Y}^{\text{sat}}(P)) \tag{8}$$
$$+ (1-\beta)/\rho_{\text{EoS}}^{\text{liq}}(T^{\text{sat}}(P) + \Delta T, P, \mathbf{X}) - \frac{Av}{\dot{m}_{\text{tot}}},$$

$$\text{res}_2 = \beta h_{\text{EoS}}^{\text{vap}}(T^{\text{sat}}(P), P, \mathbf{Y}^{\text{sat}}(P)) \tag{9}$$
$$+ (1-\beta)h_{\text{EoS}}^{\text{liq}}(T^{\text{sat}}(P) + \Delta T, P, \mathbf{X}) - h,$$

$$\text{res}_{2+i} = \beta Y_i^{\text{sat}} + (1-\beta)X_i - Z_i, \quad i = 1, \dots, N \tag{10}$$

where β is the mass fraction of vapor, superscripts vap, liq and sat refer to vapor, liquid and the saturated phase and $\mathbf{Z}, \mathbf{X}, \mathbf{Y}^{\text{sat}}$ denote the mass fractions of the total mixture, the liquid, and the saturated vapor, respectively. In the above equations, the liquid is superheated and the

vapor is saturated. For evaporating flows, $\beta = 0$ and $\mathbf{X} = \mathbf{Z}$ before the phase transition begins. For condensing flows, $\beta = 1$, $\mathbf{Y} = \mathbf{Z}$ before the phase transition begins. Moreover, for condensing flows it is the liquid that is at saturation conditions in Eqs. (8)–(10), and the vapor that is metastable.

2.2. Mathematical modeling of Zone 4

Similar to Banasiak et al. [2], we use a zero-dimensional approach to model the pre-mixing chamber in Zone 4. We here assume that the pressure at the inlet of Zone 5 (the mixer) is the same for both the primary stream (subscript I) and the secondary stream (subscript II), and that an isentropic compression/expansion takes place without any mixing of the two streams. The governing equations are then the pressure equality

$$P_{\text{I,MIX}} = P_{\text{II,MN}}, \tag{11}$$

the continuity equations

$$A_{\text{I,MIX}} v_{\text{I,MIX}} \rho_{\text{I,MIX}} = A_{\text{I,MN}} v_{\text{I,MN}} \rho_{\text{I,MN}} \tag{12}$$

$$A_{\text{II,MIX}} v_{\text{II,MIX}} \rho_{\text{II,MIX}} = A_{\text{II,SN}} v_{\text{II,SN}} \rho_{\text{II,SN}} \tag{13}$$

$$A_{\text{I,MIX}} + A_{\text{II,MIX}} = \pi D_{\text{MIX}}^2/4, \tag{14}$$

the conservation of energy

$$h_{\text{I,MIX}} + v_{\text{I,MIX}}^2/2 = h_{\text{I,MN}} + v_{\text{I,MN}}^2/2 \tag{15}$$

$$h_{\text{II,MIX}} + v_{\text{II,MIX}}^2/2 = h_{\text{II,SN}} + v_{\text{II,SN}}^2/2, \tag{16}$$

and isentropic expansion/compression:

$$s_{\text{I,MIX}} = s_{\text{I,MN}} \tag{17}$$

$$s_{\text{II,MIX}} = s_{\text{II,SN}}. \tag{18}$$

Here s is the specific entropy, the subscripts "MN" and "SN" refer to the conditions at the exit of the motive and suction nozzles, respectively, and subscript "MIX" refers to the inlet plane of Zone 5.

2.3. Mathematical modeling of Zones 5 and 6

In Zones 5 and 6, there are two streams that interact, the inner primary stream (subscript I) and the outer secondary stream (subscript II). The continuity equations for these streams are:

$$\frac{d\left(A_{\text{I}}\rho_{\text{I}}v_{\text{I}}\right)}{dz} = \frac{d\dot{m}_{\text{I,tot}}}{dz} = f_{c,\text{I}} \tag{19}$$

$$\frac{d\left(A_{\text{II}}\rho_{\text{II}}v_{\text{II}}\right)}{dz} = \frac{d\dot{m}_{\text{II,tot}}}{dz} = f_{c,\text{II}} = -f_{c,\text{I}} \tag{20}$$

$$\frac{d\left(A_I \rho_I v_I + A_{II} \rho_{II} v_{II}\right)}{dz} = \frac{d\dot{m}_{tot}}{dz} = 0 \tag{21}$$

where f_c accounts for the transfer of mass between the two streams. Furthermore, if we have a mixture, we also need to model the mass balances of $N-1$ components in stream I. The remaining masses can be deduced from an overall mass balance. The mass balances of component i are

$$\frac{d\left(A_I \rho_{i,I} v_I\right)}{dz} = f_{c,i,I}, \tag{22}$$

$$\frac{d\left(A_{II} \rho_{i,II} v_{II}\right)}{dz} = f_{c,i,II} = -f_{c,i,I}. \tag{23}$$

We assume that the mass transport between the two streams occurs via mass entrainment from the secondary to the primary stream.

The momentum balances of the streams are

$$\frac{d\left(A_I \rho_I v_I^2\right)}{dz} = -A_I \frac{dP}{dz} + f_{m,I}, \tag{24}$$

$$\frac{d\left(A_{II} \rho_{II} v_{II}^2\right)}{dz} = -A_{II} \frac{dP}{dz} + f_{m,II}, \tag{25}$$

$$\frac{d\left(A_I \rho_I v_I^2 + A_{II} \rho_{II} v_{II}^2\right)}{dz} = -A \frac{dP}{dz} + f_{m,I} + f_{m,II}. \tag{26}$$

The energy balances are

$$\frac{d\left(A_I \rho_I v_I \left(h_I + \frac{v_I^2}{2}\right)\right)}{dz} = f_{e,I}, \tag{27}$$

$$\frac{d\left(A_{II} \rho_{II} v_{II} \left(h_{II} + \frac{v_{II}^2}{2}\right)\right)}{dz} = f_{e,II} = -f_{e,I}, \tag{28}$$

$$\frac{d\left(A_I \rho_I v_I \left(h_I + \frac{v_I^2}{2}\right) + A_{II} \rho_{II} v_{II} \left(h_{II} + \frac{v_{II}^2}{2}\right)\right)}{dz} = 0. \tag{29}$$

The closure relations for these equations, $f_{c,I}, f_{m,I}, f_{m,II}, f_{e,I}$ are complicated, as the flow and interaction is highly turbulent. The approximations used in our model are based on those presented by Banasiak and Hafner [2], with some corrections and modifications.

We model entrainment from the secondary to the primary stream (II → I) as follows

$$\frac{d\Gamma_{II \to I}^{entrain}}{dz} = \begin{cases} K v_I \sqrt{\rho_I \rho_{II}} \eta_{II} (\mathrm{Re}_{II} - \mathrm{Re}_{II,\infty}) \frac{dA_{int}}{dz}, & \mathrm{Re}_{II} \geq \mathrm{Re}_{II,\infty} \\ 0, & \mathrm{Re}_{II} \leq \mathrm{Re}_{II,\infty} \end{cases} \tag{30}$$

where $\frac{dA_{int}}{dz}$ is the differential of the surface area between the streams per length, $K = 1.175 \cdot 10^{-4}$ sm/kg and

$$\mathrm{Re}_{II,\infty} = \exp\left(5.8504 + 0.4249 \frac{\eta_I}{\eta_{II}} \sqrt{\frac{\rho_{II}}{\rho_I}}\right) \tag{31}$$

This correlation for entrainment is taken from the work by Schadel et al. [28].

We neglect mass transfer by condensation/evaporation and deposition, as these mechanisms are negligible compared to entrainment in the setups considered in this work, because the time scale for heat transfer here is very small. This has been verified numerically. Thus

$$f_{c,I} = -f_{c,II} = \frac{d\Gamma_{II \to I}^{entrain}}{dz}. \tag{32}$$

It is assumed that an incipient portion of stream II is entrained, which gives

$$f_{c,i,I} = -f_{c,i,II} = w_{II} \frac{d\Gamma_{II \to I}^{entrain}}{dz}, \tag{33}$$

where w is the mass fraction.

The interface momentum transfer rate from the primary to the secondary stream is divided into two contributions: $\Pi_{I \to II}$, which assumes a uniform velocity in each stream, and $W_{f,\Delta v}$ that accounts for the velocity difference of the streams. The contributions are modeled as [2]

$$\frac{d\Pi_{I \to II}}{dz} = \frac{1}{2} \rho_I C_{I \to II} |v_I - v_{II}| (v_I - v_{II}) \frac{dA_{int}}{dz} \tag{34}$$

$$C_{I \to II} = a \mathrm{Re}_{I \to II}^{-0.25} \tag{35}$$

$$\mathrm{Re}_{I \to II} = \frac{\rho_{II}}{\eta_{II}} (v_I - v_{II}) D \left(\frac{A_I}{A_I + A_{II}}\right)^{0.5} \tag{36}$$

and

$$\frac{dW_{f,\Delta v}}{dz} = \frac{1}{2} f_{int} \rho_I (v_I - v_{II})^2 \frac{dA_{int}}{dz}. \tag{37}$$

The parameter a was fitted by Banasiak and Hafner [2] to experiments for an R744 (carbon dioxide) ejector. We provide a new value that gives a better agreement with experimental data in Table 1. Further details on the regression of these coefficients are provided in Sections 2.6 and 4.3.2.

The area-averaged velocity of the secondary stream in the z direction is by definition equal to v_{II}. However, the secondary stream velocity is expected to vary considerably in the radial direction, being zero at the wall and increasing towards the interface of the primary stream, where it reaches its highest value. To account for the wall friction arising from such a velocity profile, we divide it into two contributions: one contribution $W_{f,w}$ that accounts for the average velocity v_{II} of the secondary stream, and another contribution $W_{f,w,\Delta v}$ that accounts for the gradient of v_{II} in the radial direction, which creates additional wall shear stress. The contributions are modeled as

$$\frac{dW_{f,w}}{dz} = \frac{1}{2} f_w \rho_{II} v_{II}^2 \frac{dA_w}{dz} \tag{38}$$

and

$$\frac{dW_{f,w,\Delta v}}{dz} = \frac{dW_{f,\Delta v}}{dz} \tag{39}$$

where the last equality represents an assumption used due to the lack of detailed information about the velocity gradients through the two phases, information which would be available in e.g. CFD simulations [12].

The friction factors are in all cases calculated from the Churchill correlation, which is a function of the Reynolds number, the hydraulic diameter, and the length scale of "roughness" of the interface. The roughness of the fluid interface between the streams, ϵ_{int}, was also fitted and is given in Table 1.

Unlike previous work [2], we do not incorporate an additional friction force between the two streams, as this is an effect already accounted for in the interface momentum transfer rate.

The formulae for the hydraulic diameter of circular and annular ducts are

$$D_h^{circular} = D \tag{40}$$

$$D_h^{annular} = \frac{\pi D_o^2 - \pi D_i^2}{\pi D_o + \pi D_i} = D_o - D_i, \tag{41}$$

where D is the diameter in the circular case, and D_i and D_o are the inner and outer diameters in the annular case. The momentum closure relations take the form

$$f_{m,I} = v_{II} \frac{d\Gamma_{II \to I}^{entrain}}{dz} - \frac{d\Pi_{I \to II}}{dz} - \frac{dW_{f,\Delta v}}{dz} \tag{42}$$

$$f_{m,II} = -f_{m,I} - \frac{dW_{f,w}}{dz} - \frac{dW_{f,w,\Delta v}}{dz}. \tag{43}$$

Note that, because of Eq. (39), the friction force $\frac{dW_{f,w,\Delta v}}{dz}$ cancels out with $\frac{dW_{f,\Delta v}}{dz}$, and thus has no net effect on the secondary stream. Its effect on the primary stream is to reduce its momentum, which is ultimately due to an indirect interaction with the wall.

The energy transported by the entrained mass from stream II to stream I is

$$f_{e,I} = -f_{e,II} = \left(h_{II} + \frac{1}{2} v_{II}^2\right) \frac{d\Gamma_{II \to I}^{entrain}}{dz}. \tag{44}$$

Here we have neglected heat flow through the wall, which is in line with the assumptions made for previous zones. We have also neglected the heat flow between the two streams, since the high speeds and short

Table 1
Coefficients for interface roughness and momentum transfer.

	ϵ_{int}/μm	ϵ_w/μm	a
Zone 5	5.0	1.0	1.4
Zone 6	5.0	1.0	1.4

interaction lengths of Zones 5 and 6 render heat flow between streams insignificant.

In Zones 5 and 6, the HEM model was used within each stream to calculate thermodynamic properties, the rationale being that enough time has passed to establish local thermodynamic equilibrium.

2.4. The local exergy destruction

The local entropy production, σ, and exergy destruction, $\dot{e}_d$ in Zones 1–3 are given by the following expression:

$$\sigma = \frac{\dot{e}_d}{T_0} = \frac{\dot{m}_{tot}}{T} \left(\frac{v^2 f}{8A^2} \frac{dA_w}{dz} \right) - \sum_i^N \frac{\dot{m}_{tot,i}}{A} \left(\frac{\mu_i^{vap}}{T^{vap}} - \frac{\mu_i^{liq}}{T^{liq}} \right) \frac{d\beta_i}{dz}, \tag{45}$$

where T_0 is the ambient temperature, $\dot{m}_{tot,i}$ is the total mass flow rate of component i, μ_i is the chemical potential of component i, and β_i is the mass fraction of component i in the vapor phase, i.e. $\dot{m}_{tot,i}^{vap}/\dot{m}_{tot,i}$. The first term on the right-hand-side of Eq. (45) is viscous dissipation due to wall interaction. The second term is the entropy production from the nonequilibrium conversion between the two phases, which is zero in the HEM model. There is no exergy destruction in Zone 4 since it is assumed to be isentropic. In Zones 5–6, the local entropy production and exergy destruction are given by:

$$\begin{aligned}
\sigma = \frac{\dot{e}_d}{T_0} = &\left[-\sum_i^N w_{i,II} \left(\frac{\mu_{i,I}}{T_I} - \frac{\mu_{i,II}}{T_{II}} \right) + h_{II} \left(\frac{1}{T_I} - \frac{1}{T_{II}} \right) \right. \\
&\left. + \frac{1}{2} \frac{(v_I - v_{II})^2}{T_I} \right] \left(\frac{1}{A} \frac{d\Gamma_{II \to I}^{entrain}}{dz} \right) \\
&+ \left(\frac{v_I}{T_I} - \frac{v_{II}}{T_{II}} \right) \left(\frac{1}{A} \frac{d\Pi_{I \to II}}{dz} \right) + \left(\frac{v_I}{T_I} \right) \left(\frac{1}{A} \frac{dW_{f,\Delta v}}{dz} \right) \\
&+ \left(\frac{v_{II}}{T_{II}} \right) \left(\frac{1}{A} \frac{dW_{f,w}}{dz} \right),
\end{aligned} \tag{46}$$

where w_i is the mass fraction of component i. The above equation shows that the entropy production comes from four different terms. The first term on the right-hand-side of Eq. (46) is entropy production from entrainment, the second term comes from interfacial momentum transfer, the third and fourth term come from interfacial friction between the streams and the wall. The total exergy destruction in each zone of the ejector is:

$$\dot{E}_d = \int_0^L A(z) e_d \, dz \tag{47}$$

We shall also compare results from Eq. (47) to an overall entropy balance to verify the correctness of the above equations and implementation:

$$\frac{\dot{E}_d}{T_0} = (\dot{m}s)_{out} - (\dot{m}s)_{in} \tag{48}$$

where s is the mass specific entropy, subscripts "in" and "out" mean at the inlet and outlet of the zone respectively, and T_0 is the temperature of the environment (taken to be 293.15 K).

2.5. Calculation of thermophysical properties

Thermodynamic calculations for pure CO_2 were performed using the most accurate equations of state available (EoS), namely the multiparameter EoS of Span and Wagner [29]. The calculations with mixtures were performed using the Peng–Robinson equation of state [30]. These

EoS were interfaced by the in-house, open-source thermodynamic library Thermopack, which contains a wide selection of EoS and routines for robust phase equilibrium calculations [31–33].

For calculations in the metastable regions, care must be taken. Other relaxation approaches in the literature also use metastable phase properties with multiparameter EoS, but these properties are approximated by a linear extrapolation from the saturation state [2,34]. However, to ensure thermodynamic consistency one should rather extrapolate a thermodynamic potential as a function of its natural variables, such as the Helmholtz energy as a function of $(T, V, \mathbf{n})$, where V is the volume and $\mathbf{n}$ is the vector with the number of moles of the components, or the Gibbs energy as a function of $(T, P, \mathbf{n})$. To avoid potential consistency issues, we obtained metastable properties directly from the EoS, not by extrapolation. This was done by first locating the spinodal [24], and then using a bracketing solver between the saturation state and the spinodal state.

Thermal conductivities and viscosities of the pure components and mixtures were computed with the corresponding state approach, TRAPP, with propane as the reference fluid [35].

2.6. Regression of coefficients

Since new experimental data are available (Supplementary Material), we have re-fitted the values given in Ref. [2] of the momentum transfer parameter a between the primary and secondary stream, and the interface roughness ϵ_{int}. This is done to have a more precise representation of the pressure lift. When regressing these parameters, the objective function O was defined as the sum of the relative deviations of pressure lifts at the end of Zone 5 and Zone 6, where the total pressure lift was weighted twice as high as the intermediate pressure lift:

$$O(a, \epsilon_{int}) = \frac{1}{3} \sum_{i=1}^N \frac{|P_{5,out}^{exp} - P_{5,out}^{calc}|}{P_{5,out}^{exp} - P_{s,in}} + \frac{2}{3} \sum_{i=1}^N \frac{|P_{6,out}^{exp} - P_{6,out}^{calc}|}{P_{6,out}^{exp} - P_{s,in}} \tag{49}$$

Here $P_{5,out}^{calc}$ and $P_{6,out}^{calc}$ are the calculated pressures at the end of Zones 5 and 6, where calculations are done using the same initial conditions as the experiment i. $P_{s,in}$ is the corresponding suction inlet pressure. We included at least two experiments for each of the five ejector geometries in the objective function, but only used the $N = 12$ experiments for which the D-HRM model predicts critical mass flow to within 1% accuracy. This was to ensure that the optimal values of a and ϵ_{int} were not contaminated by inaccurate values of the critical mass flow.

3. Experiments

To validate the results from the mathematical model, we will compare numerical results to experimental results from an experimental test facility, where several ejector geometries have been investigated. Since the details of this test facility were provided in earlier work (See Fig. 3 in [2]), we will here only review the main characteristics. For ease of readability, the measurements are given in the Supplementary Material.

The ejector (Fig. 2) consists of two main body-parts manufactured as a single piece each: the motive nozzle (1) and a combination (2) of the suction nozzle, mixer, and diffuser passage. Three different geometries will be considered for the motive nozzle (1), called N1–N3, and five geometries will be considered for the remaining part of the geometry (2), called M1–M5. The advantage of this is that several ejector geometries can be tested by assembling different parts. A detailed description of these geometries can be found in the Supplementary Material.

The ejector was mounted in a specially designed test facility for analyzing the heat pump and refrigerator units. The test facility with the ejector at the center includes a receiver tank. The gas from this tank is compressed, cooled, and sent into the motive nozzle of the ejector. The liquid from the tank is regulated by a metering valve and sent through an evaporator and into the suction nozzle of the ejector. The test facility is well-equipped with temperature sensors
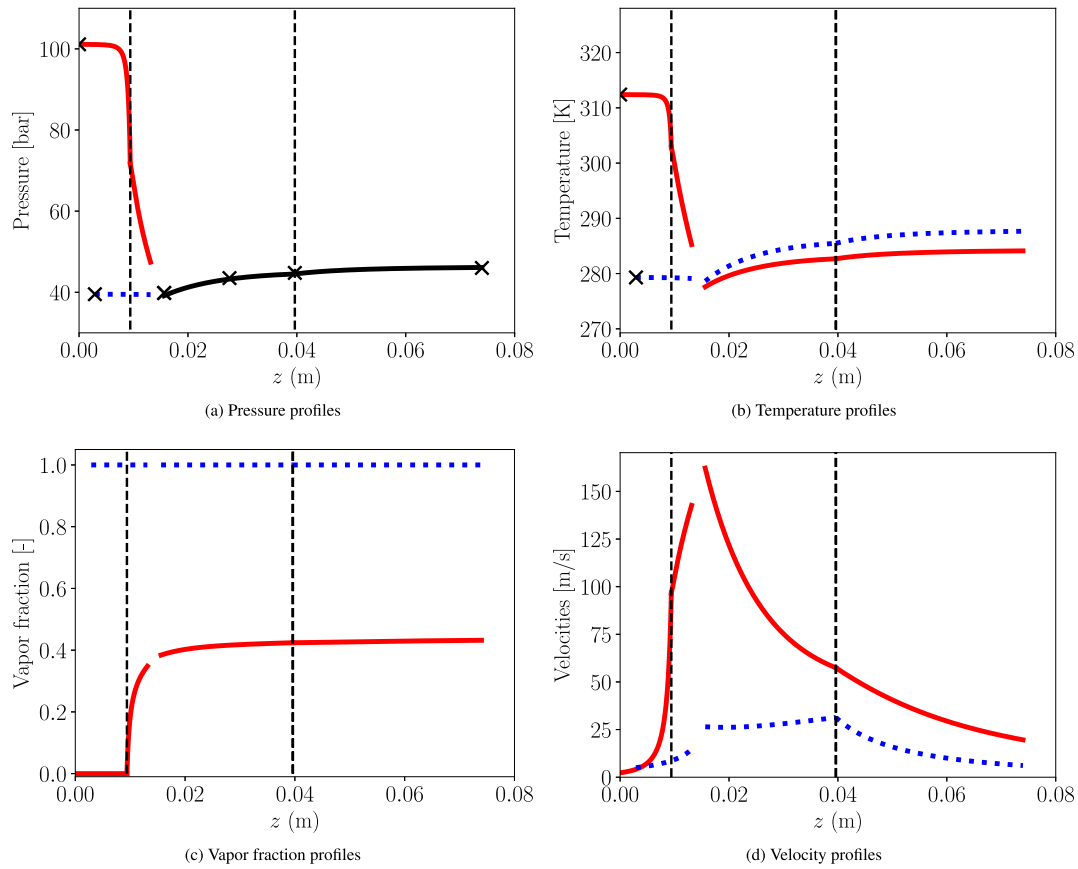
(a) Pressure profiles

(b) Temperature profiles

(c) Vapor fraction profiles

(d) Velocity profiles

Fig. 3. Local pressures, temperatures, vapor-fractions and velocities through the ejector for the Base Case defined by Table 2. Crosses represent the experimental measurements. The red solid curves are results from the primary stream, the dotted blue curves are from the secondary stream. The solid black curve in (a) is the common value of the pressure for the streams. The two vertical dashed lines mark the boundary between zones 1 and 2, and zones 5 and 6, respectively. The discontinuity in the profiles is from Zone 4.

Table 2
Inlet conditions and geometry specification for the Base Case.

Variable	Value
Fluid	CO_2
Inlet pressure motive nozzle	$10.112 \cdot 10^6$ Pa
Inlet pressure suction nozzle	$3.952 \cdot 10^6$ Pa
Inlet temperature motive nozzle	312.4 K
Inlet temperature suction nozzle	279.3 K
Entrainment ratio	0.42
Geometry specification	N3-M1

(calibrated T-type thermocouples), absolute and differential pressure sensors (calibrated piezoelectric elements), and mass flow meters (calibrated Coriolis type). The relevant experimental results are provided in the Supplementary Material.

The uncertainty in the critical mass flow rates from the experiments was discussed in a previous work [20]. We found that an uncertainty of ±1 K and ±0.3 bar in the motive fluid inlet state could translate into a ±8% uncertainty in the prediction of critical mass flow rate. It is therefore important to minimize uncertainties in the temperature and pressure sensors, and to account for this uncertainty when modeling ejectors.

4. Results

4.1. Local property profiles in the Base Case

We will first discuss the local profiles through the ejector for a specific set of inlet conditions and ejector geometry, which henceforth will be referred to as the "Base Case". The details that specify the

Base Case are presented in Table 2, and the fluid examined is CO_2. The entrainment ratio (0.42) is defined as the ratio between the inlet massflow rate into the suction nozzle and the inlet massflow rate into the motive nozzle. More details on the ejector geometry can be found in the Supplementary Material.

For the Base Case, the critical mass flow rate is underpredicted by 0.28% whereas the pressure lift is overpredicted by 1.8%; both values are within the experimental uncertainty (the experimental values can be found in the Supplementary Material). The local profiles from the Base Case are depicted in Fig. 3, including a comparison of measurements through the ejector (crosses). All of the profiles have a discontinuity in the domain 0.013 m < z < 0.016 m. This domain is Zone 4, the pre-mixing chamber, which in the present model is represented by a set of algebraic equations that only give the outlet state. Hence, the local property profiles in Zone 4 are not provided by the model, only the inlet and outlet states.

In the experimental facility described in Section 3, pressures were measured at intermediate positions in the ejector. Fig. 3(a) shows that these pressures are predicted to a high accuracy by the model. While the secondary stream enters as vapor and remains in the single-phase regime through the ejector, the primary stream enters the two-phase regime at the throat of the motive nozzle, after which vapor forms rapidly (see Fig. 3(c)). In Section 2, two methods were presented to describe the transition from one phase to two phases in the motive nozzle, the homogeneous equilibrium model (HEM) and the delayed homogeneous relaxation model (D-HRM). In HEM, the two-phase transition occurs precisely when the coexistence curve is reached. In D-HRM, however, the transition is delayed until the limit of superheat is encountered. Although D-HRM gives, in general, more accurate results as we will demonstrate in Section 4.3, both methods give accurate predictions
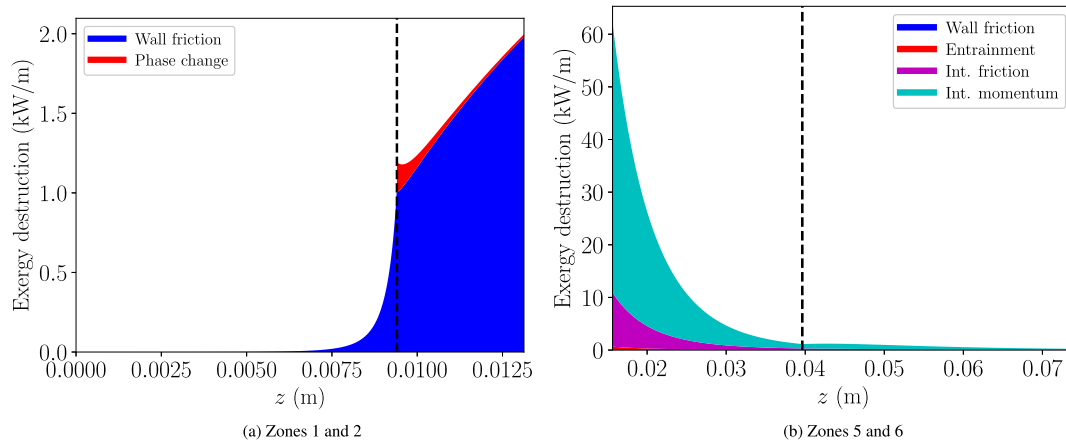
(a) Zones 1 and 2

(b) Zones 5 and 6

Fig. 4. The local exergy destruction spatially through the ejector decomposed into different contributions for the D-HRM model. Here the vertical dashed lines separate Zones 1 and 2 (left) and Zones 5 and 6 (right). A more detailed explanation of the different sources of exergy destruction can be found in Section 2.4.

of the critical mass flow rate for the Base Case. The reason why HEM works well for the Base Case, is that the inlet temperature is very close to the critical temperature of CO_2 (304.13 K). In vicinity of the critical point, the limit of superheat is close to the two-phase coexistence curve, and there is little difference in the predictions from HEM and D-HRM.

The velocities of both the primary and secondary streams increase prior to Zone 4. After Zone 4, the velocities converge towards a common value due to the vigorous momentum exchange and friction between the streams after the pre-mixing chamber (see Fig. 3(d)).

4.2. The local exergy destruction of the Base Case

A general shortcoming of ejectors is their low efficiency. To increase this efficiency, it is of key importance to uncover where and how useful work is lost inside the ejector through exergy destruction/entropy production. We will next use the methodology presented in Section 2.4 to compute the local exergy destruction through the ejector for the Base Case and discuss the underlying mechanisms and how they can be mitigated.

The integral defined in Eq. (47) was compared to the overall entropy balance presented in Eq. (48), and the equations were found to agree with the desired numerical accuracy. This was a consistency check carried out to ensure correct implementation of the computational routines to calculate the exergy destruction, as well as a check of correctness of the formulae in Eqs. (45) and (46).

Fig. 4 displays the local exergy destruction in Zones 1 and 2 (Fig. 4(a)) and in Zones 5 and 6 (Fig. 4(b)), where the vertical dashed lines mark the end of one zone and the start of another. In Zone 1, the exergy destruction originates in wall friction, which increases rapidly towards the throat due to the increased velocity. This exergy destruction comes from the first term on the right-hand-side of Eq. (45). Formation of vapor is initiated at the throat, which leads to exergy destruction as the fluid relaxes towards the two-phase equilibrium conditions. This is the last term on the right-hand-side of Eq. (45). The exergy destruction in Zone 3, the suction nozzle, is negligible due to the low velocities (see Fig. 3) and has therefore not been shown. Fig. 4(a) shows that the largest source of exergy destruction in Zones 1 and 2 is wall friction, albeit the nonequilibrium transition to two phases is also significant. Note that the exergy destruction from phase change will be zero with the HEM, which causes a slight underprediction of the exergy destruction for this model.

Zone 4 has been assumed to be isentropic, which means that there is no exergy destruction. This is clearly a questionable assumption, since there is significant exergy destruction in all adjacent zones. However, a closer inspection of Fig. 3(a) shows that the pressure at the outlet of Zone 4 is reproduced to a high accuracy by the model. We expect

that if there were a significant exergy destruction in Zone 4, the predicted pressure would differ more from what is measured. Future work, e.g. comparison to CFD simulations is needed to shed further light on this.

The largest exergy destruction in the ejector can be found in Zone 5, the mixer, and is shown in Fig. 4(b). The exergy destruction at the inlet of Zone 5 exceeds 60 kW/m, while the maximum exergy destruction in Zone 2 is about 2 kW/m. The major portion of the exergy destruction in Zone 5 originates in transport of momentum from the primary stream to the secondary stream, i.e. the second contribution on the right-hand-side of Eq. (46). The second-largest contribution to the exergy destruction comes from friction between the interface of the primary and secondary streams, i.e. the third contribution on the right-hand-side of Eq. (46). The exergy destruction from entrainment is barely visible at the inlet of Zone 5. The exergy destruction from wall friction is not visible in the figure. The reason for this is that the wall is in contact with the secondary stream, which has a modest velocity and a low density throughout the ejector, as shown in Fig. 3(d).

The exergy destruction is mostly decaying through Zones 5 and 6, although there is a slight increase at the inlet of the diffuser. The total exergy destruction in the mixer is much larger than that of the diffuser. The ejector efficiency of the Base Case, is 21.7%, as defined by the formula by Elbel and Hrnjak [3]. In the Base Case, a total of 357 W of useful work is dissipated as exergy destruction throughout the ejector. Improving the efficiency of ejectors should focus on reducing the exergy destruction, and the dominating part is the mixer (Zone 5).

In the literature, equipartition of the local entropy production has been shown to characterize energy efficient process equipment. This applies to a wide variety of examples, ranging from heat exchangers [10], to distillation columns [9], chemical reactors [36] and even reindeer noses [37]. Equipartition of the entropy production is equivalent with equipartition of the local exergy destruction, or in other words, an exergy destruction that is evenly distributed through the ejector.

With a near-exponential decay through Zone 5, the exergy destruction profiles, and thus also the local entropy production profiles, are very far from evenly distributed. Indeed, the profiles shown in Fig. 4 are characteristic of an *energy inefficient* process equipment. There is no reason why the mixer should have a constant diameter, albeit without any clear guidelines on how to improve the design of the ejector, a constant diameter appears to be a sensible first approach. The model and tools presented in this work provide a solid basis to develop geometric designs for ejectors that give a lower exergy destruction, and thus higher efficiency. This is an interesting possibility for future work.

Table 3

Statistics for the relative deviations in predicted critical motive mass flow rate for HEM and D-HRM for the CO_2 experiments shown in Figs. 5(a) and 5(b).

Model	Bias	MAPE	Max error
D-HRM (evaporation)	−1.6%	2.6%	9.0%
HEM (evaporation)	−8.4%	8.4%	34.3%
D-HRM (condensation)	−0.7%	0.8%	2.6%
HEM (condensation)	−0.8%	0.9%	2.9%

Table 4

Statistics for the relative deviations in critical mass flow rate and pressure lift for D-HRM with optimal values of the interface roughness and momentum transfer parameter. The statistics have been calculated for the conditions shown in Figs. 5(c) and 5(d).

Model	Bias	MAPE	Max error
Pressure lift	0.8%	2.3%	9.0%
Motive mass flow	0.6%	1.4%	4.1%

4.3. A comparison of the model to results for pure CO_2 – new experiments

After establishing that the ejector model reproduces the experimental results of the Base Case to a high accuracy in Section 4.1, we now proceed to discuss its performance for other experiments where CO_2 is used as working fluid. In these experiments, several inlet conditions and the geometries have been investigated. The relevant experimental data are provided in the Supplementary Material.

4.3.1. Prediction of critical mass flow rates

We first discuss the ability of the ejector model to reproduce critical mass flow rates from experiments, as this is crucial for reliable prediction of the pressure lift and efficiency of the ejector [2]. We showed in a previous paper that D-HRM can significantly improve predictions of critical mass flow for evaporating flows in comparison to HEM [20]. A common denominator for all comparisons made in Ref. [20] was that evaporation was initiated in the nozzle throat, and formation of vapor was the limiting factor for further increase in the critical mass flow rate. An illustration is provided in Fig. 5(a), which shows that while HEM exceedingly underpredicts the critical mass flow rates at lower temperatures, D-HRM moves the predictions closer to the experimental data. Below $T = 285$ K, D-HRM tends towards overpredicting the critical mass flow rate. The reason for this is that there is a crossover between homogeneous and heterogeneous nucleation at this temperature, as discussed in detail in Ref. [20]. Since we in the remaining part of this work will discuss experiments with inlet temperatures above $T = 290$ K, we can safely rely on homogeneous nucleation theory. This has the advantage that no fitting parameters are needed.

For condensing flows, the picture is simpler. If the inlet temperature of the motive nozzle is sufficiently far above the critical temperature, condensation in the throat and the associated latent heat release will be the limiting factor to further increase the critical mass flow rate. A comparison to the new measurements of condensing flows is shown in Fig. 5(b). Unlike evaporating flows, both HEM and D-HRM reproduce the experimental data within their accuracy. The reason for this is presumably that the homogeneous nucleation limit of condensation lies much closer to the coexistence curve than that of evaporation (see Fig. 2 in Ref. [20]). Note that different geometries were used for evaporating and condensing flows, the reason being that these are the only campaigns that cover a substantial region of the phase envelope.

The statistics of the experiments shown in Figs. 5(a)–5(b) are given in Table 3. The table shows that both models work well for condensing flows, whereas only D-HRM is satisfactory for evaporating flows.

Fig. 5(c) compares the D-HRM model to the additional experimental data reported in the Supplementary Material. These data represent thermodynamic states that are in vicinity of the critical point of CO_2. The figure shows that the experiments are reproduced to a high accuracy, with a Mean Absolute Percentage Error (MAPE) of 1.4% and a maximum error of 4.1%, as shown in Table 4. The bias is defined as the mean percentage error without taking absolute values. For evaporation the bias shows that HEM consistently underpredicts the experimental results while the error for D-HRM is more evenly distributed; for condensation, both models generally underpredict.

4.3.2. Prediction of pressure lifts

Using the new experimental data, we have re-fitted the values of the momentum transfer parameter a between the primary and secondary stream, and the interface roughness ϵ_{int}, to have a more precise representation of the pressure lift. Details on the algorithm used in this regression can be found in Section 2.6. The resulting coefficients were presented in Table 1. We found that it was possible to use the same parameters in Zones 5 and 6, which reduces the adjustable parameters from four to two in comparison to previous work [2]. Interestingly, the value obtained for the interface roughness, $\epsilon_{int} = 5\,\mu m$, is significantly higher than that of Banasiak and Hafner [2], who used the values $2\,\mu m$ and $4\,\mu m$ in Zones 5 and 6, respectively.

For the experiments considered, the pressure lifts were reproduced with a MAPE of 2.3% and a maximum error of 9.0%, as shown in Table 4. An overview of all the experiments from five different geometries for the mixer and diffuser, M1-M5, are displayed in Fig. 5(d). The exact dimensions of these ejector geometries can be found in the Supplementary Material.

4.4. Extending the discussion to mixtures

The ejector model has thus far been used to examine ejectors with streams consisting of pure CO_2. Although the vast majority of the literature on ejectors deals with single-component fluids, it is well-known that the use of mixed refrigerants has the potential to greatly improve the performance of refrigeration cycles. We shall next discuss the influence of including more components in the fluid on the ejector performance, while keeping the inlet conditions and ejector geometry fixed.

Since we have found that HEM gives accurate predictions for the Base case, we assume that this also applies when including a minute concentration of a second component. For simplicity, we have therefore used HEM when studying mixtures. Furthermore, we have used the same parameter values for the interface roughness and momentum transfer as for pure CO_2 (see Table 1). Apart from this, all other properties have been taken for the specific mixtures by use of an in-house thermodynamic library, as elaborated in Section 2.5.

Using the Base Case from Section 4.1 as starting point, we have included a minute concentration of a second component, with an equal mole fraction in the primary and secondary stream. The two components SO_2 and H_2 have been chosen for illustrative purposes. Fig. 6 compares the phase envelopes of a CO_2 mixture with 0.3% H_2 (dashed line) and 3.0% SO_2 (dash–dot line). While the phase envelope of the CO_2-H_2 mixture lies above the saturation curve of pure CO_2 (solid line), the phase envelope of CO_2-SO_2 lies below.

A comparison of the ejector performance with the CO_2-H_2 and CO_2-SO_2 mixtures is presented in Fig. 7. While adding SO_2 increases the critical mass flow rate, the opposite can be seen for H_2 (see Fig. 7(a)). This can be explained from the phase envelopes depicted in Fig. 6. Since addition of SO_2 shifts the bubble points to lower pressures relative to pure CO_2, a more substantial expansion can take place prior to phase change. This translates into a higher critical mass flow rate. The opposite is true for H_2, since the bubble points are shifted to higher pressures than for pure CO_2. The model suggests that adding only 2% H_2 to the CO_2 will lead to a 20% reduction in the critical mass flow rate. Even though the increase in the critical mass flow rate is modest when the mole fraction of SO_2 is increased to 2%, the pressure lift increases
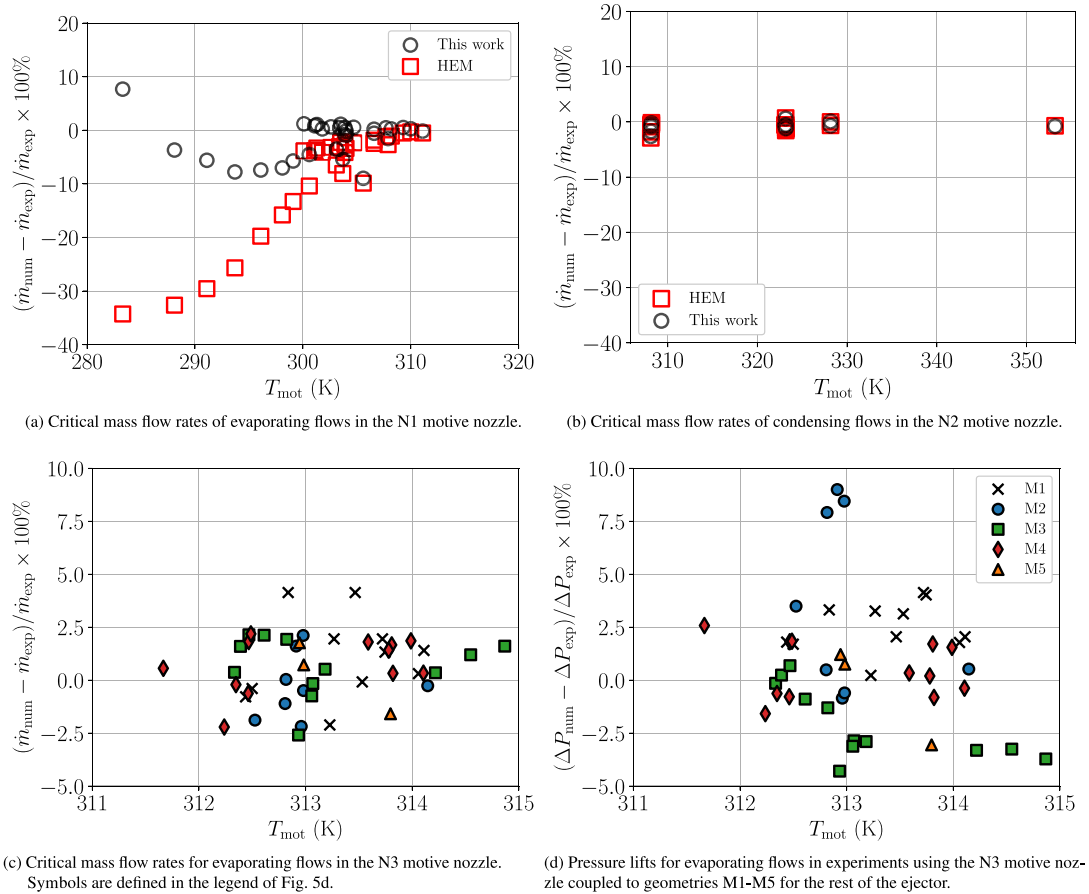
(a) Critical mass flow rates of evaporating flows in the N1 motive nozzle.

(b) Critical mass flow rates of condensing flows in the N2 motive nozzle.

(c) Critical mass flow rates for evaporating flows in the N3 motive nozzle. Symbols are defined in the legend of Fig. 5d.

(d) Pressure lifts for evaporating flows in experiments using the N3 motive nozzle coupled to geometries M1-M5 for the rest of the ejector.

Fig. 5. Panels a and b: Percentage deviation of critical mass flow of HEM and D-HRM from measurements. (a) Evaporating flows in the N1 motive nozzle, where the experiments are published in Banasiak and Hafner [38]. (b) Condensing flows in the N2 motive nozzle, where the measurements are reported in Table 3 in the Supplementary Material. Panels c and d: Comparison of simulated and experimental critical mass flow rates (c) and pressure lift (d) reported in the Supplementary Material for the N3 motive nozzle.
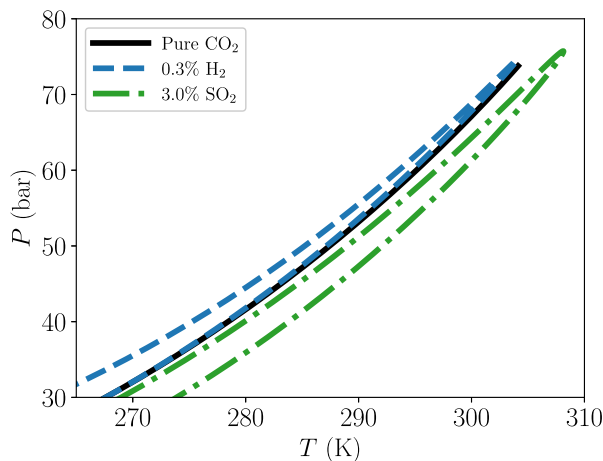

Fig. 6. Phase envelopes in temperature–pressure space for pure CO_2, and for its binary mixtures with 0.3 mole percentage H_2 and 3.0 mole percentage SO_2.

by more than 1 bar. This is significant, since the pressure lift of the Base Case is ~6.5 bar (see Fig. 7(b)).

Although the pressure lift increases with the addition of SO_2, the ejector efficiency drops from above 21% to below 10%, as shown in Fig. 7(c). This is also reflected in the total exergy destruction through the ejector (see Fig. 7(d)). It is not surprising that the efficiency of the ejector decreases when applied to different mixtures, since this ejector geometry was originally designed for CO_2. The loss of efficiency

is connected to the kink seen in the pressure-lift, efficiency and total exergy destruction profiles at about 0.75% SO_2 in Fig. 7(c). This kink is caused by condensation in the suction nozzle (Zone 3), which causes a large decrease in the performance. This loss of performance can probably be mitigated by modifying the design of the ejector.

The results above reveal that the performance of ejectors can be improved by a suitable choice of mixture, accompanied by a tailormade design of the ejector geometry.

4.5. Further work

As we showed in previous work [20], the D-HRM model significantly improves the accuracy in the prediction of critical mass flow rates. In the vicinity of the critical point of fluids, homogeneous classical nucleation theory can be used to predict the nucleation limit and the method is fully predictive. At lower temperatures, however, there is a cross-over to heterogeneous nucleation. The theoretical basis to predict the nucleation limit governed by heterogeneous nucleation theory, e.g. when bubbles are formed in cracks, needs to be further developed before the D-HRM model is fully predictive at temperatures significantly below the critical point of a fluid. An alternative to this is to extract the heterogeneous nucleation limit from experiments, as done for water in Ref. [20].

Only inlet temperatures close to the critical point of the fluid were used in the regression of the momentum transfer parameter a between the primary and secondary stream, and the interface roughness ϵ_{int}. Experimental data for CO_2 at lower temperatures are needed to validate and extend the applicability of the presented model. Furthermore, experimental data for other fluids than CO_2 are needed to develop a
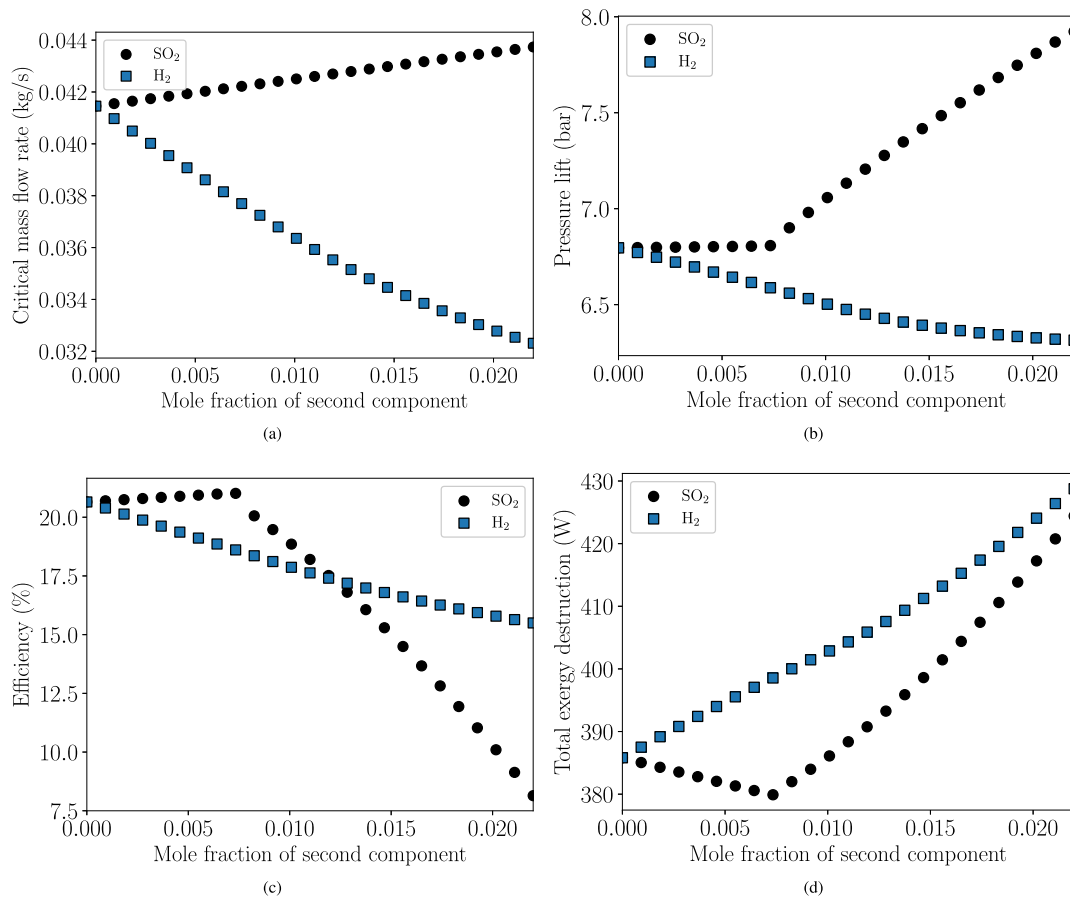
Fig. 7. The ejector performance of mixtures with CO_2-H_2 and CO_2-SO_2 at different compositions. The mole fraction of the second component is the same in both inlet streams, and the geometry and inlet conditions are the same as in the Base Case (see Section 4.1 for details). HEM has been used to describe the two-phase transition in the motive nozzle.

general correlation for a and ϵ_{int}, possibly based on the principle of corresponding states.

Even when an ejector cycle is designed to operate with a pure working fluid such as CO_2, there are many potential sources of impurities: e.g. air leaks and dissolved lubricant from turbomachinery. Seeing as Fig. 7 demonstrates that even small amounts of impurity have a dramatic impact on ejector performance, it is clear that further work on mixtures is needed.

5. Conclusion

We have presented a one-dimensional ejector model for mixtures, with spatially distributed mass-, energy- and momentum-balances for the different zones that together constitute the full ejector geometry. Furthermore, new experimental results for pure CO_2, both for critical mass flow rates through nozzles, and for pressure lift through five different ejector geometries, were used to improve the accuracy of the model.

The recently developed delayed homogeneous relaxation model (D-HRM) was incorporated in the ejector model to describe the two-phase transition in the motive nozzle. The performance of D-HRM was compared to the homogeneous equilibrium model (HEM), which assumes full equilibrium at all times. For experiments where evaporation in the throat of the motive nozzle limits the critical mass flow rate, D-HRM gave an average deviation of 2.6%. This was significantly more accurate than HEM, which gave an average deviation of 8.4% for the experiments considered.

We presented new experimental data where the critical mass flow rate in the ejector was governed by condensation in the throat of the motive nozzle. Both D-HRM and HEM were in excellent agreement

with the experimental data, with average deviations below 0.9%. The reason for this is that the limit of metastability in the liquid-phase is much closer to the coexistence curve than the corresponding limit in the vapor-phase, which leads to very similar results for D-HRM and HEM. We expect this to be true, not only for CO_2, but for other fluids as well.

New experimental data on the pressure lifts from five different ejector geometries were used to improve the correlation for the momentum transfer between the primary and secondary streams, yielding a model that reproduces the pressure lift within 2.3% on average. For CO_2, more data are required at lower temperatures to validate and extend the applicability of the model.

By using nonequilibrium thermodynamics, we have derived formulae for the local exergy destruction in the ejector. This allowed us to determine the nature and location of the loss of useful work in the form of exergy destruction. For the case examined, we showed that the vast majority of the exergy destruction was in the mixer. Most of this exergy destruction originated in friction and momentum transfer between the primary and secondary stream. The local exergy destruction displayed a rapidly decaying profile, which is far from uniformly distributed. Since equipartition of the local exergy destruction is an established guideline for energy-efficient design of process equipment, this reveals a large potential for improvement, e.g. by modifying the design and geometry of the ejector.

Assuming that the model validated for pure CO_2 could also be used for mixtures rich in CO_2, the applicability of the model in handling mixtures was demonstrated by investigating the influence of including a second impurity into the CO_2. While including SO_2 causes an increase in the critical mass flow rate, including H_2 causes a reduction. We showed that by adding only 2% H_2 to the mixture, the critical mass flow rate dropped by more than 20%. Furthermore, 2% addition of

SO_2 increased the pressure-lift by 1 bar, albeit the ejector efficiency was shown to decrease. These examples show that the use of mixtures in ejectors can be used as a leverage to improve their performance. Experimental data on ejector operation with mixtures are needed to validate these predictions and further develop the model.

Declaration of competing interest

The authors declare that they have no known competing financial interests or personal relationships that could have appeared to influence the work reported in this paper.

Data availability

Data will be made available on request.

Appendix A. Supplementary data

Supplementary material related to this article can be found online at https://doi.org/10.1016/j.applthermaleng.2022.119228.

References

[1] G. Besagni, R. Mereu, F. Inzoli, Ejector refrigeration: a comprehensive review, Renew. Sustain. Energy Rev. 53 (2016) 373–407.

[2] K. Banasiak, A. Hafner, 1D computational model of a two-phase R744 ejector for expansion work recovery, Int. J. Therm. Sci. 50 (2011) 2235–2247.

[3] S. Elbel, P. Hrnjak, Experimental validation of a prototype ejector designed to reduce throttling losses encountered in transcritical R744 system operation, Int. J. Refrig. 31 (2008) 411–422.

[4] F. Liu, Review on ejector efficiencies in various ejector systems, in: Proceedings of the International Refrigeration and Air Conditioning Conference, 2014.

[5] E. Bellos, C. Tzivanidis, Optimum design of a solar ejector refrigeration system for various operating scenarios, Energy Convers. Manage. 154 (2017) 11–24.

[6] G. Alexis, E. Karayiannis, A solar ejector cooling system using refrigerant R134a in the athens area, Renew. Energy 30 (9) (2005) 1457–1469.

[7] S. Kjelstrup, D. Bedeaux, Non-Equilibrium Thermodynamics of Heterogeneous Systems, World Scientific, Singapore, 2008.

[8] E. Johannessen, S. Kjelstrup, A highway in state space for reactors with minimum entropy production, Chem. Eng. Sci. 60 (12) (2005) 3347–3361.

[9] D. Kingston, Ø. Wilhelmsen, S. Kjelstrup, Minimum entropy production in a distillation column for air separation described by a continuous non-equilibrium model, Chem. Eng. Sci. 218 (2020) 115539.

[10] R. Hånde, Ø. Wilhelmsen, Minimum entropy generation in a heat exchanger in the cryogenic part of the hydrogen liquefaction process: on the validity of equipartition and disappearance of the highway, Int. J. Hydrog. Energy 44 (29) (2019) 15045–15055.

[11] G. Skaugen, D. Berstad, Ø. Wilhelmsen, Comparing exergy losses and evaluating the potential of catalyst-filled plate-fin and spiral-wound heat exchangers in a large-scale claude hydrogen liquefaction process, Int. J. Hydrog. Energy 45 (11) (2020) 6663–6679.

[12] J. Sierra-Pallares, J.G. Del Valle, P.G. Carrascal, F.C. Ruiz, A computational study about the types of entropy generation in three different R134a ejector mixing chambers, Int. J. Refrig. 63 (2016) 199–213.

[13] A. Arbel, A. Shklyar, D. Hershgal, M. Barak, M. Sokolov, Ejector irreversibility characteristics, J. Fluids Eng. 125 (1) (2003) 121–129.

[14] E. Lakzian, M. Hajian, A. Farahmand, The entropy generation rate minimization for a proposed air ejector for the carpet industry, Meccanica 53 (1) (2018) 145–159.

[15] F. Foroozesh, A.B. Khoshnevis, E. Lakzian, Investigation on the effects of water steam ejector geometry in the refrigeration systems using entropy generation assessment, J. Therm. Anal. Calorim. (2019) 1–13.

[16] T. He, N. Mao, Z. Liu, M.A. Qyyum, M. Lee, A.M. Pravez, Impact of mixed refrigerant selection on energy and exergy performance of natural gas liquefaction processes, Energy 199 (2020) 117378.

[17] C. Reddick, M. Sorin, H. Sapoundjiev, Z. Aidoun, Effect of a mixture of carbon dioxide and steam on ejector performance: An experimental parametric investigation, Exp. Therm Fluid Sci. 92 (2018) 353–365.

[18] T. Bai, G. Yan, J. Yu, Experimental investigation of an ejector-enhanced auto-cascade refrigeration system, Appl. Therm. Eng. 129 (2018) 792–801.

[19] K.E. Ringstad, Y. Allouche, P. Gullo, Å. Ervik, K. Banasiak, A. Hafner, A detailed review on co2 two-phase ejector flow modeling, Therm. Sci. Eng. Prog. (2020) 100647, http://dx.doi.org/10.1016/j.tsep.2020.100647.

[20] Ø. Wilhelmsen, A. Aasen, Accounting for the nucleation limit is key for accurate prediction of critical mass flow rates through constrained geometries, Chem. Eng. Sci. 248 (2022) 117176.

[21] H.A. Jakobsen, Elements of Chemical Reaction Engineering, Springer, 2014.

[22] M.M. Awad, Y.S. Muzychka, Effective property models for homogeneous twophase flows, Exp. Therm. Fluid Sci. 33 (2008) 106–113.

[23] S.W. Churchill, Friction factor equation spans all fluid flow regimes, Chem. Eng. 84 (1977) 91–92.

[24] P. Aursand, M.A. Gjennestad, E. Aursand, M. Hammer, Ø. Wilhelmsen, The spinodal of single-and multi-component fluids and its role in the development of modern equations of state, Fluid Phase Equilib. 436 (2017) 98–112, http://dx.doi.org/10.1016/j.fluid.2016.12.018.

[25] Ø. Wilhelmsen, D. Bedeaux, S. Kjelstrup, D. Reguera, Thermodynamic stability of nanosized multicomponent bubbles/droplets: The square gradient theory and the capillary approach, J. Chem. Phys. 140 (2) (2014) 024704, http://dx.doi.org/10.1063/1.4860495.

[26] A. Aasen, E.M. Blokhuis, Ø. Wilhelmsen, Tolman lengths and rigidity constants of multicomponent fluids: fundamental theory and numerical examples, J. Chem. Phys. 148 (20) (2018) 204702, http://dx.doi.org/10.1063/1.5026747.

[27] A. Aasen, D. Reguera, Ø. Wilhelmsen, Curvature corrections remove the inconsistencies of binary classical nucleation theory, Phys. Rev. Lett. 124 (2020) 045701, http://dx.doi.org/10.1103/PhysRevLett.124.045701.

[28] S. Schadel, G. Leman, J. Binder, T. Hanratty, Rates of atomization and deposition in vertical annular flow, Int. J. Multiph. Flow 16 (3) (1990) 363–374.

[29] R. Span, W. Wagner, A new equation of state for carbon dioxide covering the fluid region from the triple-point temperature to 1100 K at pressures up to 800 MPa, J. Phys. Chem. Ref. Data 25 (1996) 1509.

[30] D.Y. Peng, D.B. Robinson, A new two-constant equation of state, Ind. Eng. Chem. Fund. 15 (1976) 59, http://dx.doi.org/10.1021/i160057a011.

[31] Ø. Wilhelmsen, A. Aasen, G. Skaugen, P. Aursand, A. Austegard, E. Aursand, M.A. Gjennestad, H. Lund, G. Linga, M. Hammer, Thermodynamic modeling with equations of state: Present challenges with established methods, Ind. Eng. Chem. Res. 56 (13) (2017) 3503–3515, http://dx.doi.org/10.1021/acs.iecr.7b00317.

[32] A. Aasen, M. Hammer, G. Skaugen, J.P. Jakobsen, Ø. Wilhelmsen, Thermodynamic models to accurately describe the $PVTxy$-behavior of water/carbon dioxide mixtures, Fluid Phase Equilib. 442 (2017) 125–139, http://dx.doi.org/10.1016/j.fluid.2017.02.006.

[33] Ø. Wilhelmsen, G. Skaugen, M. Hammer, P.E. Wahl, J.C. Morud, Time efficient solution of phase equilibria in dynamic and distributed systems with differential algebraic equation solvers, Ind. Eng. Chem. Res. 52 (2013) 2130.

[34] W. Angielczyk, Y. Bartosiewicz, D. Butrymowicz, J.-M. Seynhaeve, 1-d modeling of supersonic carbon dioxide two-phase flow through ejector motive nozzle, in: International Refrigerant and Air Conditioning Conference, 2010, pp. 1–8, URL http://docs.lib.purdue.edu/iracc/1102.

[35] M. Baltatu, R. Chong, M. Huber, Viscosity of defined and undefined hydrocarbon liquids calculated using an extended corresponding-states model, Int. J. Thermophys. 17 (1) (1996) 213–221.

[36] Ø. Wilhelmsen, E. Johannessen, S. Kjelstrup, Energy efficient reactor design simplified by second law analysis, Int. J. Hydrogen Energy 35 (2011) 13219–13231.

[37] E. Magnanelli, Ø. Wilhelmsen, M. Acquarone, L.P. Folkow, S. Kjelstrup, The nasal geometry of the reindeer gives energy-efficient respiration, J. Non-Equilib. Thermodyn. 42 (1) (2017) 59–78.

[38] K. Banasiak, A. Hafner, Mathematical modelling of supersonic two-phase R744 flows through converging–diverging nozzles: The effects of phase transition models, Appl. Therm. Eng. 51 (1–2) (2013) 635–643.